[Rock and Soil Mechanics](https://rocksoilmech.researchcommons.org/journal)

Volume 44 | Issue 7 Article 1

11-3-2023

# Mode I crack morphology and fracture surface roughness of granite under impact

Xue-song WANG
*School of Architecture and Civil Engineering, Shenyang University of Technology, Shenyang, Liaoning 110870, China*, wangxs@smail.sut.edu.cn

Lian-jun GUO
*School of Architecture and Civil Engineering, Shenyang University of Technology, Shenyang, Liaoning 110870, China*

Xin LIU
*College of Mining Engineering, University of Science and Technology Liaoning, Anshan, Liaoning 114051, China; Engineering Research Center of Green Mining of Metal Mineral Resources of Liaoning Province, Anshan, Liaoning 114051, China*

Ding DENG
*School of Architecture and Civil Engineering, Shenyang University of Technology, Shenyang, Liaoning 110870, China*

*See next page for additional authors*



## Recommended Citation

WANG, Xue-song; GUO, Lian-jun; LIU, Xin; DENG, Ding; ZHANG, Jiu-yang; and XU, Zhen-yang (2023) "Mode I crack morphology and fracture surface roughness of granite under impact," *Rock and Soil Mechanics*: Vol. 44: Iss. 7, Article 1.
DOI: 10.16285/j.rsm.2022.6209
Available at: https://rocksoilmech.researchcommons.org/journal/vol44/iss7/1

# Mode I crack morphology and fracture surface roughness of granite under impact


## Abstract

To study the response of mode I cracks under impact loading, the dynamic fracture test on the single cleavage triangle (SCT) granite specimens with the lateral opening was carried out using a split Hopkinson pressure bar test system. The Hough transform method was used to quantitatively describe the distributions of the surface crack lengths and angles, and the relationship between them and the absorbed energy of the specimen was analyzed. The three-dimensional (3D) point cloud data of the fracture surface was obtained by using a 3D surface topography detection device, and a fracture surface reconstruction method based on the threshold detection of the fitting surface was proposed, which effectively solved the error problem caused by the appearance of error points in the 3D point cloud data of the fracture surface. The relationship between fracture surface roughness and absorbed energy was also discussed. The results show that the exponential distribution of crack length $\lambda$ tends to increase, and the distribution of crack angles is more even with the increase in absorbed energy. There are relatively few cracks in the horizontal direction, and the cracks have obvious directionality when the dissipated energy of the specimen is lower, while the bending degree of the cracks is higher and the connectivity is better when the dissipated energy is higher. The fracture surface reconstruction method can complete the fracture surface processing better at 0.03-0.08 of the points in the x and y directions and the threshold of 0.25. The roughness statistical parameters of fracture surfaces A and B showed a decreasing trend with the increase in dissipated energy.



## Keywords

single cleavage triangle (SCT) specimen, rock fracturing, Hough transform, fracture surface roughness, mode I crack



## Authors

Xue-song WANG, Lian-jun GUO, Xin LIU, Ding DENG, Jiu-yang ZHANG, and Zhen-yang XU

Rock and Soil Mechanics 2023 44(7): 1925–1936 ISSN 1000−7598
https: //doi.org/10.16285/j.rsm.2022.6209 http://rocksoilmech.researchcommons.org/journal

# Mode I crack morphology and fracture surface roughness of granite under impact

WANG Xue-song[1], GUO Lian-jun[1], LIU Xin[2, 3], DENG Ding[1], ZHANG Jiu-yang[2, 3], XU Zhen-yang[2, 3]
1. School of Architecture and Civil Engineering, Shenyang University of Technology, Shenyang, Liaoning 110870, China
2. College of Mining Engineering, University of Science and Technology Liaoning, Anshan, Liaoning 114051, China
3. Engineering Research Center of Green Mining of Metal Mineral Resources of Liaoning Province, Anshan, Liaoning 114051, China

**Abstract:** To study the response of mode I cracks under impact loading, the dynamic fracture test on the single cleavage triangle (SCT) granite specimens with the lateral opening was carried out using a split Hopkinson pressure bar test system. The Hough transform method was used to quantitatively describe the distributions of the surface crack lengths and angles, and the relationship between them and the absorbed energy of the specimen was analyzed. The three-dimensional (3D) point cloud data of the fracture surface was obtained by using a 3D surface topography detection device, and a fracture surface reconstruction method based on the threshold detection of the fitting surface was proposed, which effectively solved the error problem caused by the appearance of error points in the 3D point cloud data of the fracture surface. The relationship between fracture surface roughness and absorbed energy was also discussed. The results show that the exponential distribution of crack length $\lambda$ tends to increase, and the distribution of crack angles is more even with the increase in absorbed energy. There are relatively few cracks in the horizontal direction, and the cracks have obvious directionality when the dissipated energy of the specimen is lower, while the bending degree of the cracks is higher and the connectivity is better when the dissipated energy is higher. The fracture surface reconstruction method can complete the fracture surface processing better at 0.03−0.08 of the points in the $x$ and $y$ directions and the threshold of 0.25. The roughness statistical parameters of fracture surfaces A and B showed a decreasing trend with the increase in dissipated energy.

**Keywords:** single cleavage triangle (SCT) specimen; rock fracturing; Hough transform; fracture surface roughness; mode I crack

## 1 Introduction

In geotechnical engineering such as mine, water conservancy and tunnel, dynamic fracture of rock mass is often triggered by blasting and other dynamic loads, resulting in instability and failure of underground structures[1]. As a heterogeneous material, rock contains a large number of defects and fissures that determine the crack morphology after fracture under dynamic loading[2−3]. Therefore, it is of great significance to study the dynamic characteristics and crack propagation laws of rock materials under impact loading.

Split Hopkinson pressure bar (SHPB) test system is widely used for dynamic impact loading test to analyze the response, crack propagation and energy dissipation characteristics of materials under impact loading[4−7]. By using the improved single cleavage semi-circle (ISCSC) specimen configuration, Wang et al.[8] studied the overall process of crack propagation and termination under impact loading. Cao et al.[9] investigated the dynamic fracture of single cleavage drilled compression (SCDC) specimens, and recorded the times of dynamic initiation, propagation, termination and secondary initiation of cracks. Ni et al.[10−11] studied the dynamic fracture toughness and stress intensity factors of SCDC specimens and double cleavage drilled compression (DCDC) plates under impact loading. In general, using specimens with pre-existing cracks to study the crack propagation under impact loading has become the dominant method in this field. Among them, the single cleavage triangle (SCT) specimen adopted by Dong et al.[12−13] not only facilitates the study of the crack growth law, but also has the advantages of simple structure and easy processing, and it has also been adopted in the research of Wang et al.[14−15].

Previous studies focused on the whole propagation process of mode I crack, especially the initiation, termination and secondary initiation. However, statistical studies on crack propagation patterns have been rarely reported, which can be quantitatively studied by the Hough transform method. This method was proposed by Hough[16] and allows the detection of specific shapes in image space using the duality of line−point in the parameter space, including straight line[17], circle[18], ellipse[19], etc. For the detection of crack images, David et al.[20] developed

Received: 4 August 2022 Accepted: 6 December 2022
This study was supported by the National Natural Science Foundation of China (51974187), Foundation for Key Teacher by University of Science and Technology Liaoning (601011507-25) and the Educational Commission of Liaoning Province of China (LJKZ0282).
First author: WANG Xue-song, male, born in 1995, PhD candidate, majoring in the research of rock fragmentation and numerical simulation.
E-mail: wangxs@smail.sut.edu.cn
Corresponding author: XU Zhen-yang, male, born in 1982, PhD, Associate Professor, research interests: mine blasting engineering.
E-mail: xuzhenyang10@foxmail.com

the FracPaq toolbox based on Matlab software and conducted the relevant research. Rizzo et al.[21−22] adopted the FracPaq toolbox to analyze the scanning electron microscope (SEM) crack images of sandstones, and used the two-dimensional (2D) continuous wavelet transform method to analyze the directional changes of cracks at different scales. In the subsequent studies, statistical functions such as maximum likelihood estimation and K-S test were added to the toolbox and then applied to the investigation of crack distribution of fractured rock mass in the Santa Cruz area, USA[22].

In addition, the research on the fracture surface roughness of rocks after dynamic fracture has not attracted enough attention, although the quantitative characterization of structural surface roughness has been studied for about half a century[23]. The main debates focus on the influence of roughness on the rock mass under shear effect[24−26], while there are few studies on the influence of roughness on the rock mass under impact loading. Therefore, the fracture characteristics of SCT specimens under impact loading can be investigated with the aid of existing quantitative indices of rock fracture surface roughness.

During the acquisition of fracture surface roughness, according to different detection principles, the detection devices are classified into probe contact[23], photogrammetric[27] and optical types[28]. Among them, the fracture surface roughness detection method based on the optical principle possesses the advantages of high-precision and non-damage to the structural plane[23], with the measurement accuracy even reaching nanometer level. However, in the point cloud data of fracture surface obtained by optical devices, some obvious error points are inevitable, which brings inconvenience to the subsequent processing. The reasons for these error points are as follows: (1) In the case of high precision, there is an upper limit of the measurement range in the vertical direction of the detection device. For specimens with excessive roughness, the recorded data of individual points may exceed this range, resulting in a large gap between the recorded value and the actual value. (2) The high transparency of the individual particles in the rock specimen can easily cause the scattering of the detector light source, making the detector unable to capture the reflected light source. This phenomenon has not attracted enough attention yet.

To address the above problems, in this study, the impact test on the SCT granite specimens is carried out using the SHPB test system. The Hough transform method is adopted to quantitatively describe the morphology of mode I crack. The relationship between the impact pressure and the statistical results of the distributions of crack lengths and angles is expounded, and the fracture surface reconstruction method of fitting surface inversion is proposed. The problem of error points in the three-dimensional (3D) point cloud data of fracture surface is solved, and the relationship between rock fracture surface roughness and air pressure is discussed, which provides a valuable reference for the study of rock dynamic fracture.

## 2 Test system and principle

### 2.1 Specimen preparation

The granite specimens used in the test were sampled from the Dagushan Iron Mine in Anshan, China. All the specimens were taken from an intact rock mass with a good homogeneity. The physico-mechanical parameters of rock specimens are listed in Table 1. The SCT rock sample proposed by Dong et al.[12] was used to prepare the specimens in a rectangular configuration with a triangular opening. The prefabricated crack was located at the apex of the triangle. The processed granite specimen is 50 mm wide, 100 mm high and 30 mm thick. A prefabricated crack of 10 mm in length was cut by a 1 mm thick saw blade and then sharpened. The pad is a triangular body made of steel (density of 7.9 g /cm$^3$), with a top angle of 30º, a bottom length of 16.0 mm, a height of 29.6 mm and a thickness of 30.0 mm. The structural size of the SCT specimen is illustrated in Fig. 1.

### 2.2 Test device and schemes

The SHPB test system at the University of Science and Technology Liaoning was adopted in this test, as shown in Fig. 2. The lengths of the incident bar, transmitted bar and absorbing bar are 2 100 mm, 1 800 mm and 800 mm, respectively. Both the striker and the weight bar are made of high-strength steel with a diameter of 50 mm and an elastic modulus of 210 GPa. The 3D roughness detection was performed using the PS50 profilometer produced

**Table 1 Physico-mechanical parameters of rock specimens**

| Specimen ID | Diameter /mm | Height /mm | Density /(g • cm$^{-3}$) | Compressive strength /MPa | Elastic modulus /GPa | Deformation modulus /GPa | Poisson’s ratio |
|---|---|---|---|---|---|---|---|
| 1 | 50.08 | 100.65 | 2.64 | 168.46 | 46.25 | 32.23 | 0.28 |
| 2 | 50.06 | 100.44 | 2.65 | 156.57 | 43.95 | 20.76 | 0.27 |
| 3 | 49.41 | 100.60 | 2.64 | 147.32 | 42.55 | 20.18 | 0.14 |
| 4 | 50.03 | 100.47 | 2.65 | 159.40 | 41.06 | 23.12 | 0.28 |
| 5 | 50.06 | 100.49 | 2.64 | 159.69 | 39.71 | 16.25 | 0.31 |
| Mean value | 49.93 | 100.53 | 2.64 | 158.29 | 42.70 | 22.50 | 0.26 |

https://rocksoilmech.researchcommons.org/journal/vol44/iss7/1
DOI: 10.16285/j.rsm.2022.6209

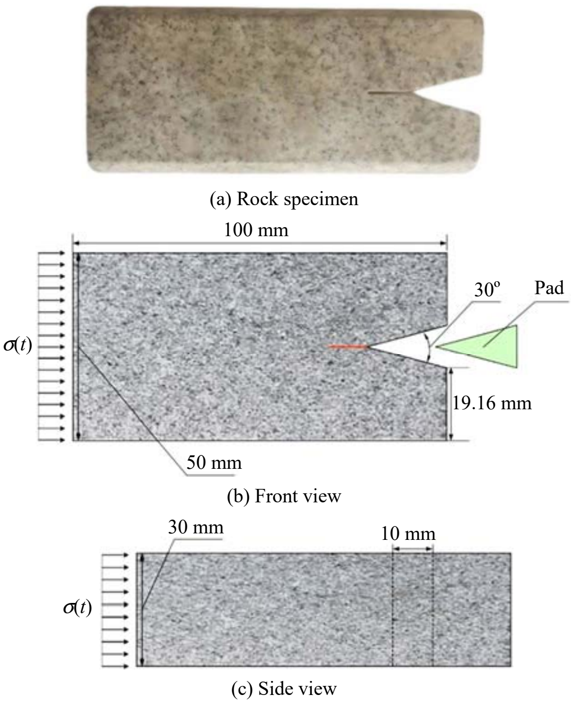


(a) Rock specimen

(b) Front view

(c) Side view

**Fig. 1 SCT specimen**

by NANOWEA company in the USA. The horizontal automatic scanning range is 50 mm, the scanning step size is 0.1 μm, and the scanning speed is 20 mm /s.

During testing, the specimen embedded with the pad is placed between the incident bar and the transmitted bar. The side of the pad is connected with the incident bar, and the side of the specimen is connected with the transmitted bar. The air pressures in the test were set to 0.2, 0.3, 0.4, 0.5 and 0.6 MPa. After the impact fracture of the specimen, the fracture surface of the specimen was scanned by a 3D topography detection equipment to generate the 3D point cloud data of fracture surface.

Before testing, a typical test was performed to check the stress equilibrium. Figure 3(a) shows the typical stress wave pattern of a tested rock specimen, and the incident wave, transmitted wave and reflected wave can meet the test requirements. Figure 3(b) illustrates the typical stress equilibrium test curve, indicating the requirements of stress equilibrium during dynamic loading.

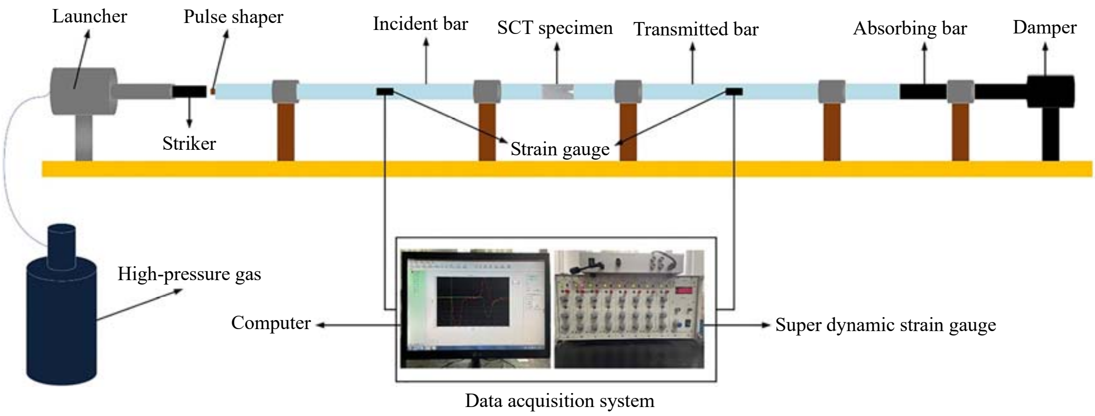


**Fig. 2 Split Hopkinson pressure bar testing system**

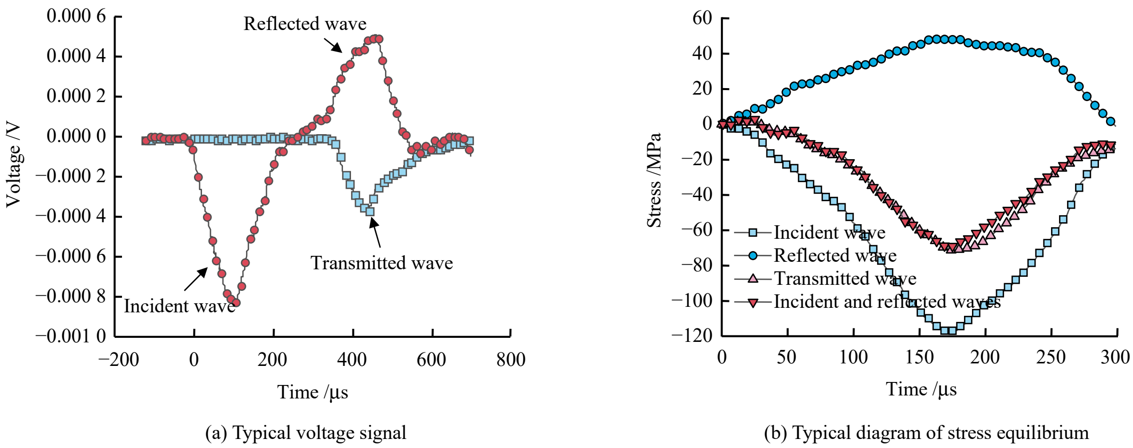


(a) Typical voltage signal

(b) Typical diagram of stress equilibrium

**Fig. 3 Trial experiment and dynamic stress equilibrium**

### 2.3 Calculation of energy dissipation

In the SHPB test, the spindle-shaped striker is launched by the high-pressure gas and gains the kinetic energy to impact the incident bar. The kinetic energy of the striker is converted into incident energy. The incident bar impacts the rock specimen, in which process the incident energy is converted into reflected energy, absorbed energy of the specimen and transmitted energy through the specimen. By ignoring the kinetic energy of rock fragments and the heat exchange between the rock and outside, the energy composed of three parts can be calculated according to the law of conservation of energy[29]:

$$\left.\begin{aligned} W_{\mathrm{i}} &= \frac{A_0 C_0}{E_0}\int \sigma_{\mathrm{i}}^2 \mathrm{d}t = A_0 E_0 C_0 \int \varepsilon_{\mathrm{i}}^2 \mathrm{d}t \\ W_{\mathrm{r}} &= \frac{A_0 C_0}{E_0}\int \sigma_{\mathrm{r}}^2 \mathrm{d}t = A_0 E_0 C_{\mathrm{b}} \int \varepsilon_{\mathrm{r}}^2 \mathrm{d}t \\ W_{\mathrm{t}} &= \frac{A_0 C_0}{E_0}\int \sigma_{\mathrm{t}}^2 \mathrm{d}t = A_0 E_0 C_0 \int \varepsilon_{\mathrm{t}}^2 \mathrm{d}t \end{aligned}\right\} \tag{1}$$

where $W_{\mathrm{i}}$, $W_{\mathrm{r}}$ and $W_{\mathrm{t}}$ represent the incident energy, reflected energy and transmitted energy, respectively; $A_0$ and $E_0$ are the sectional area and elastic modulus of the bar, respectively; $C_0$ is the longitudinal wave velocity; $\sigma_{\mathrm{i}}$, $\sigma_{\mathrm{r}}$ and $\sigma_{\mathrm{t}}$ correspond to the stresses in the incident bar, reflected bar and transmitted bar, respectively; $\varepsilon_{\mathrm{i}}$, $\varepsilon_{\mathrm{r}}$ and $\varepsilon_{\mathrm{t}}$ represent the strains of the incident bar, reflected bar and transmitted bar, respectively; and $t$ is the corresponding time.

The energy absorbed by the specimen $W_{\mathrm{d}}$ can be calculated by

$$W_{\mathrm{d}} = W_{\mathrm{i}} - W_{\mathrm{r}} - W_{\mathrm{t}} \tag{2}$$

The energy density index $w_{\mathrm{s}}$ is introduced to evaluate the absorption of energy in rock using following equation:

$$w_{\mathrm{s}} = \frac{W_{\mathrm{d}}}{V} = \frac{A_0 E_0 C_0}{A_{\mathrm{s}} l_{\mathrm{s}}}\int\left[\varepsilon_{\mathrm{i}}(t)^2 - \varepsilon_{\mathrm{r}}(t)^2 - \varepsilon_{\mathrm{t}}(t)^2\right]\mathrm{d}t \tag{3}$$

where $V$ is the volume of the specimen; $A_{\mathrm{s}}$ is the sectional area of the specimen; and $l_{\mathrm{s}}$ is the length of the specimen.

On this basis, Wang et al.[29] proposed the energy time density at peak point to evaluate the rock energy dissipation under impact loading, and its calculation formula is written as

$$w_{\mathrm{td}}(t) = \frac{w_{\mathrm{s}}(t_{\mathrm{p}})}{t_{\mathrm{p}}} \tag{4}$$

where $t_{\mathrm{p}}$ is the moment when the peak point of energy time density appears; $w_{\mathrm{s}}(t_{\mathrm{p}})$ is the energy consumption density at the time $t_{\mathrm{p}}$; and $w_{\mathrm{td}}(t)$ is the modified calculation method of energy time density.

## 3 Processing of point cloud data and crack image

### 3.1 Error points removal of point cloud data

When detecting the rock fracture surface roughness, the detection principle of the testing equipment is to extract and process the point cloud data of the fracture surface. Due to the limitation of equipment measuring range and the test conditions, there are often obvious error points during testing, which affect the quantitative results of rock fracture surface roughness. Among the commonly used statistical methods, the root-mean-square-based quantitative statistical method evaluate the fracture surface roughness based on the elevation of the calculated section in vertical direction, as shown in Fig. 4. The error points will cause the errors in the results of roughness characterization indices such as $Z_{2\mathrm{s}}$ [25] and $R_{\mathrm{p}}$ [30–31]. The Delaunay triangulation algorithm converts the cloud data into a large number of triangles for subsequent calculation, and the existence of error points results in the distortion of triangles, which is also the main cause of errors in statistical results.

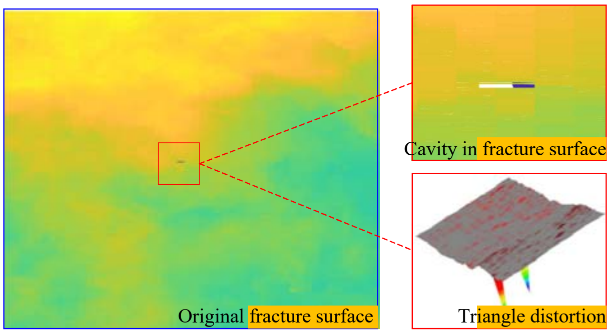


**Fig. 4 Influence of error point on fracture surface**

### 3.2 Construction of fitting surface

When the point cloud data are used to construct a surface, a plane (***x***, ***y***) is first constructed as the domain boundary, and each data point should be located in the matrix mesh of the surface in the domain. For a node at a certain position in the matrix mesh, there are generally three methods to calculate the value of this point: nearest interpolation method, trilinear interpolation, and bilinear interpolation. Based on these three methods, the value of each point can be predicted according to the local value in the mesh, so that the validity of each data point can be guaranteed. In the fitting process, it is generally acknowledged that the mesh is essentially composed of lower-order splines, and then the behavior of a given node in the mesh becomes the interpolation problem of a linear combination, which can be described by linear algebra as follows:

$$\boldsymbol{A}\boldsymbol{x} = \boldsymbol{y} \tag{5}$$

where the length of the vector $\boldsymbol{x}$ is equal to $n_x \cdot n_y$ ($n_x$ and $n_y$ are the numbers of the nodes in the $x$ and $y$ directions). Therefore, $\boldsymbol{A}$ is a coefficient matrix with $n$ rows, corresponding to each data point $n_x \cdot n_y$ in the fracture surface point cloud.

The essence of surface fitting is to deal with a regularization problem, which makes the (first) partial derivatives of the surface in the adjacent elements equal at the data points, and then produces the second set of linear equations described in the following form:

$$\boldsymbol{Bx} = \boldsymbol{0} \tag{6}$$

where the derivative is approximated by the finite difference method or Laplace transform method on the surface on adjacent nodes. First, the matrices $\boldsymbol{A}$ and $\boldsymbol{B}$ are scaled so that each matrix has a norm of 1, and then the vector $\boldsymbol{x}$ is solved to minimize the following equation:

$$\| (\boldsymbol{Ax} - \boldsymbol{y}) \|^2 + \lambda \| \boldsymbol{Bx} \|^2 \tag{7}$$

where $\lambda$ is the adjustment coefficient and its value is 1. Therefore, in the fitting process, it is necessary to set the numbers of nodes $n_x$ and $n_y$ required for fitting in the $x$ and $y$ axes in the independent mesh. The number of points in the $x$ and $y$ directions affects the number of meshes in the fitting surface. The correlation between the number of points and the number of meshes obtained is shown in Fig. 5(a). In the positive direction of both axes, the number of meshes increases with the increase in number of points. Theoretically, the finer the mesh on the surface, the better the reproduction of the fracture surface, and the validity of all point cloud data can therefore be guaranteed; otherwise, the triangle distortion shown in Fig. 4 will occur.

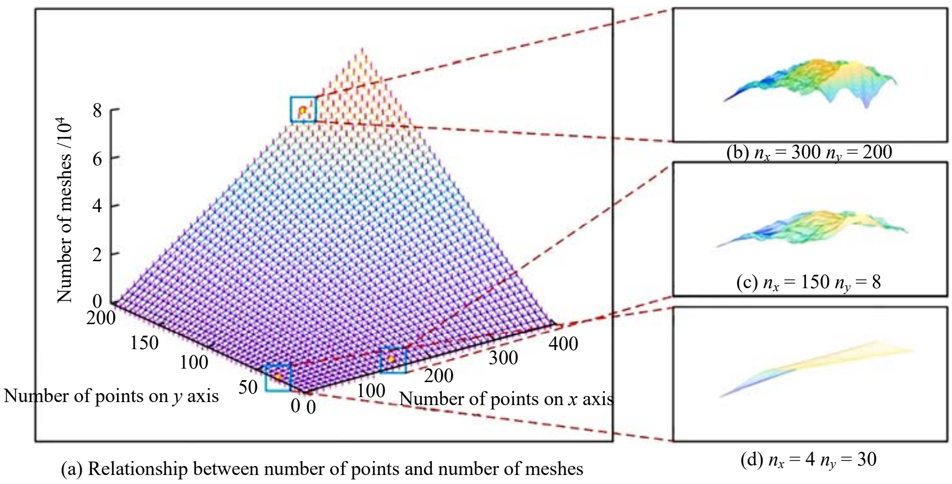


**Fig. 5 Relationship between number of points and number of grids in $x$ and $y$ axes**

The fracture surface roughness of the specimen under the impact load of 0.2 MPa was identified, and three sets of data with different node numbers on the $x$ and $y$ axes were selected for surface fitting, as presented in Fig. 5(b), 5(c) and 5(d). In Fig. 5(b), the numbers of nodes in the two directions are 300 and 200. The number of meshes has reached 6 000, and the meshes are relatively dense. However, it has been found that the error data have an impact on the results. The mesh shape at the edge of the fracture surface is irregular, indicating that the fitting surface results are greatly affected by the error point data, and the current selection of the node number is unreasonable. In Fig. 5(d), the numbers of nodes in the two directions are 4 and 30, and the number of meshes decreases to 120. Such a scarce mesh number suggests that the fitting surface can only represent the macro-level trend of the fracture surface, thereby losing a great deal of the details of rock fracture surface. Obviously, the setting of the value in Fig. 5(d) is far from the research goal. Among the three groups of tests, the more reasonable values are the results with the numbers of nodes being 8 and 150 and the number of meshes being 1 200. It can be clearly seen from Fig. 5(c) that the results of the fitting surface can effectively avoid the influence of error points without losing details. In the original point cloud data of fracture surface under the impact load of 0.2 MPa, there are 3 000 data points in the $x$ direction and 200 data points in the $y$ direction. Therefore, the reasonable range for the number of nodes in the two directions is 0.03−0.08 of the total number of point clouds in the corresponding direction.

### 3.3 Reconstruction of fracture surface data

According to the above method, the fitting surface is obtained, as shown in Fig. 6(a). The number of nodes in the $x$ and $y$ directions is set to 0.03−0.08 of the total number of points in the corresponding direction. Because the number of points on the fitting surface is much less than the actual point cloud data, it is inconvenient to compare the fitting surface with the original point cloud data. Before comparing the two groups of matrices, the matrices should be expanded by referring to the fitting results, and the data difference method was adopted to keep the numbers of rows and columns of the surface the same as that of the original point cloud data matrix, as shown in Fig. 6(b). The reconstructed point cloud data are all located on the fitted surface. The difference between the expanded matrix and the original point cloud data was calculated. The distribution of the absolute values of the difference at each position in the matrix is shown in Fig. 6(d), and it physically measures the distance between the original data and the fitting surface. In the further processing of point cloud data, the threshold can be set according to the absolute value of the difference between the two matrices. The deletion principle is that when the absolute difference is greater than the threshold, the data at this point will be deleted and replaced with the data point on the fitting surface.

Figure 7(a) shows the original distribution of the thresholds. The statistical histogram of absolute differences is shown in Fig. 7(b). The proportion of absolute differences less than 0.5 is as high as 80%, indicating a small proportion of error points in the original data. In Fig. 7(c), the distribution of error points inside the rock fracture surface is relatively scattered, and the high absolute differences are concentrated at the edge, indicating a high probability of error points appearing at the edge of the fracture surface. Figure 7(d) shows the relationship between

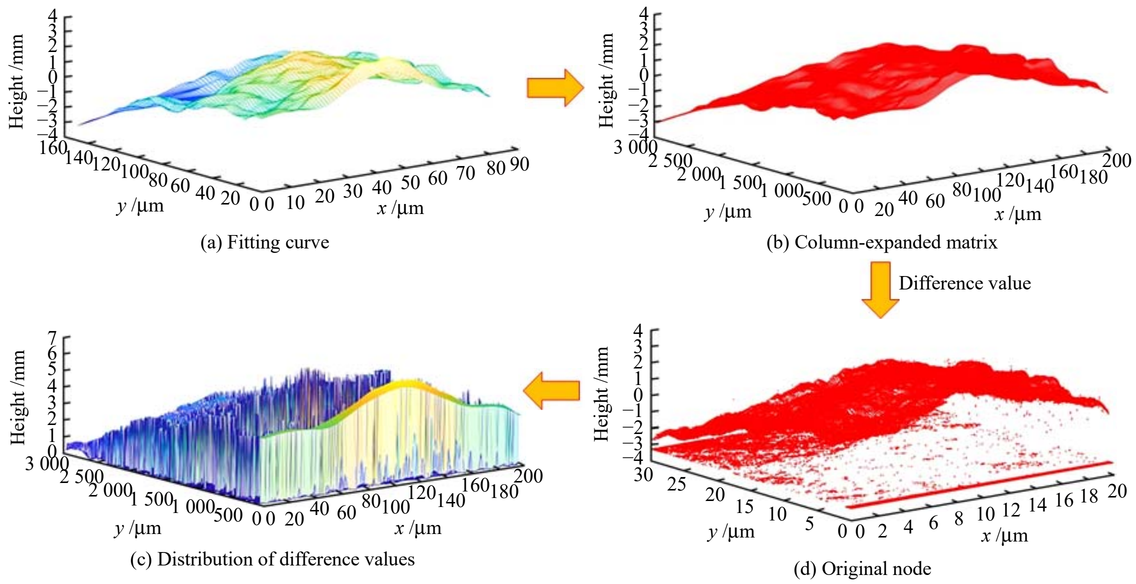


**Fig. 6 Reconstruction process of fracture surface data**

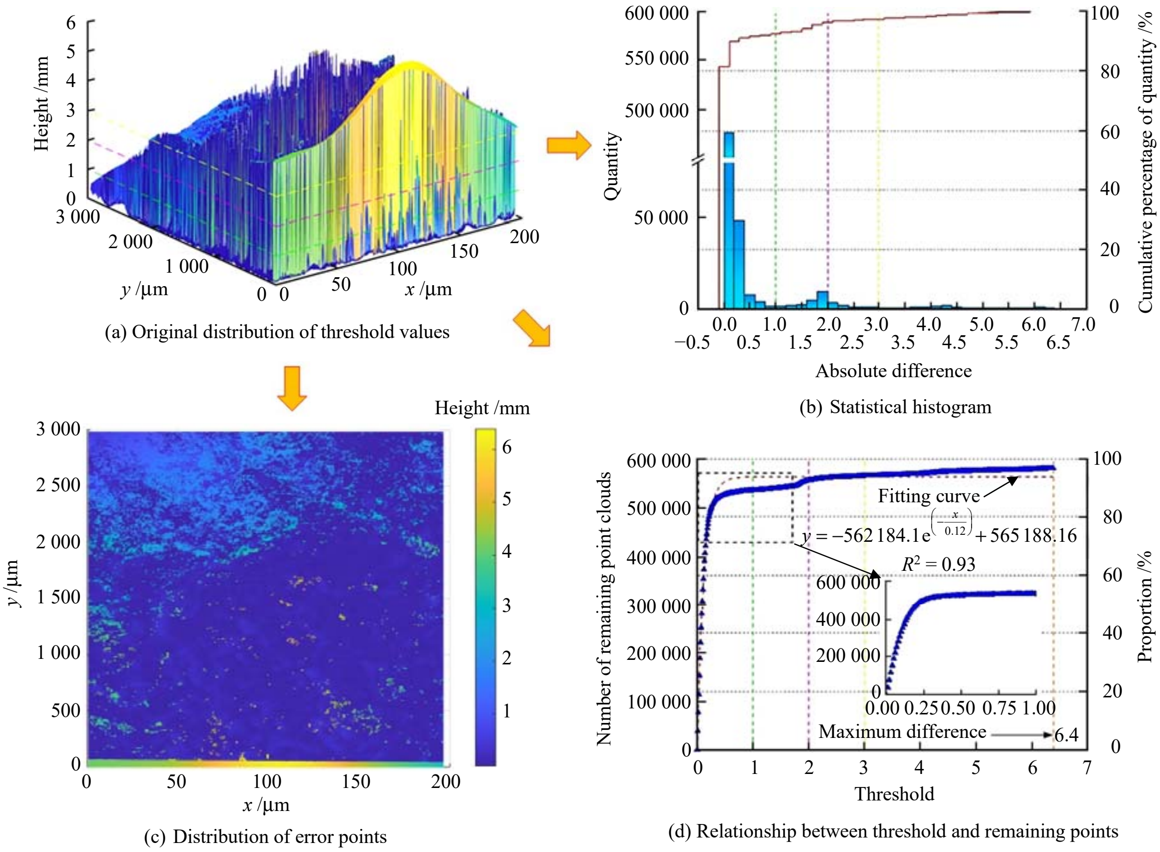


**Fig. 7 Threshold setting**


DOI: 10.16285/j.rsm.2022.6209

the thresholds and the remaining points in the point cloud data. In terms of the overall trend, the remaining points increase significantly at the initial stage when the values are less than 1, and most of the error values are within the threshold range from 0 to 1. When the threshold is greater than 2, the change of the remaining points is approximately similar to the line parallel to the $x$ axis, and the proportion of the remaining points exceeds 80%. A power function is used to fit the data points as follows:

$$y = -562\,184.1\mathrm{e}^{\left(-\frac{x}{0.12}\right)} + 565\,188.16,\ R^2 = 0.93 \qquad (8)$$

A closer look at the threshold within 0−1 reveals that the fitting curve tends to be parallel to the $x$ axis when the threshold is 0.25. Admittedly, there are some errors in the interpolation of the fitting surface. Considering that the purpose of filtering is to replace large absolute difference points, a certain error value is acceptable. Therefore, the absolute difference of 0.25 can be selected as the threshold to achieve the removal of error points.

### 3.4 Crack image processing method

The Hough transform method proposed by Paul Hough is adopted to process the crack propagation morphology, as shown in Fig. 8(a). After obtaining the image of crack region in the rock specimen, the image is binarized for processing. Then, the binarized image is processed by Hough transform for quantitative crack statistics.

As shown in Fig. 8(b), in the test, each fractured specimen is divided into left and right regions, i.e. region A and region B. The cracks corresponding to the front and back sides are termed A1, A2 and B1, B2, i.e. A1 and A2 coalesce in region A, and B1 and B2 coalesce in region B. The angles between the central axis and the cracks A1, A2, B1 and B2 are $\theta_{A1}$, $\theta_{A2}$, $\theta_{B1}$ and $\theta_{B2}$, respectively.

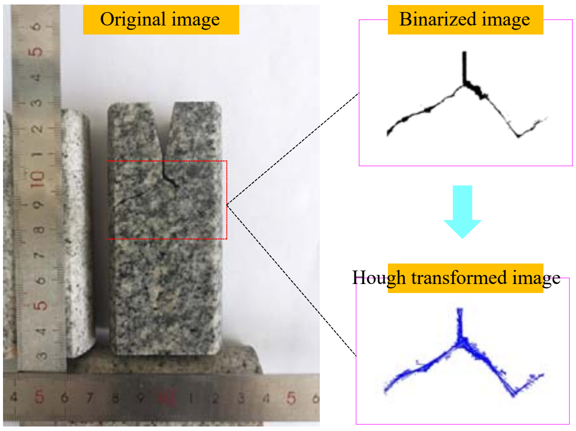


(a) Diagram of the Hough transform

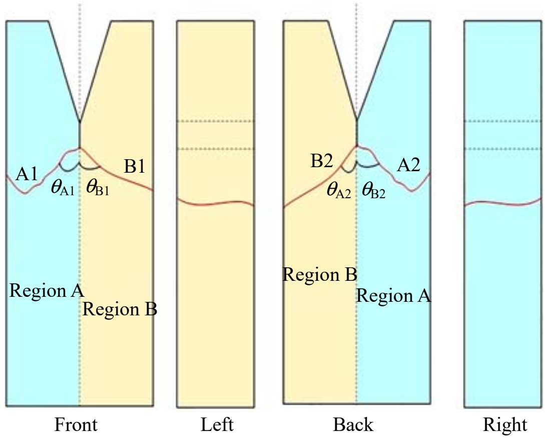


(b) Region division

**Fig. 8 Crack image processing method**

## 4 Analyses of crack morphology and fracture surface

### 4.1 Effect of impact load on crack length distribution

The general rule of the test results is that the main crack of each group initiates from the base of the pre-fabricated crack, and propagates in the transverse direction rather than the vertical direction, which is somewhat different from the observations by Dong et al.[13] and Wang et al.[8]. In the study of Wang et al.[8], tight sandstone was selected as the test material, and it was found that the density of rock materials and the composition of large particles affect the crack propagation behavior. The difference between our test results and the previous ones is that the heterogeneity of the rock leads to the deviation of the crack propagation path.

The crack images and maximum likelihood statistical results are shown in Fig. 9. After scale conversion, each pixel in the images is 0.1 mm in size. The results suggest that the larger the value of $\lambda$, the fewer the large values of $x$. The $\lambda$ value of each group fluctuates between 0.018 and 0.030, indicating that the overall crack distributions under different test conditions are similar. After observing the crack images of the front and back sides, it is found that in the first 4 groups of tests, the difference of $\lambda$ value is only about 0.01, indicating that the specimen has a certain degree of symmetry and fracture uniformity during the fracturing. In comparison, the difference of $\lambda$ in group 2 test with energy time density of 0.005 42 J /(cm$^3$ • μs) is 0.04. The reason for this is that there is an obvious gap on the left side of the front of the specimen, while the gap is smaller on the back of the specimen. For the last group, the energy time density is 0.012 93 J /(cm$^3$ • μs), and the difference of $\lambda$ is as high as 0.12. The difference in macrocrack morphology is not obvious, but the symmetry of the cracks on both sides is poor, and the fracture surface is heterogeneous, resulting in a large gap of $\lambda$ in this group. In Fig. 9(f), $\lambda$ gradually increases with the increase in energy time density, suggesting that the number of cracks in the specimen also tends to increase with the increase in absorbed energy.

Figure 10 shows the statistical distribution of crack

Rock and Soil Mechanics, Vol. 44 [2023], Iss. 7, Art. 1



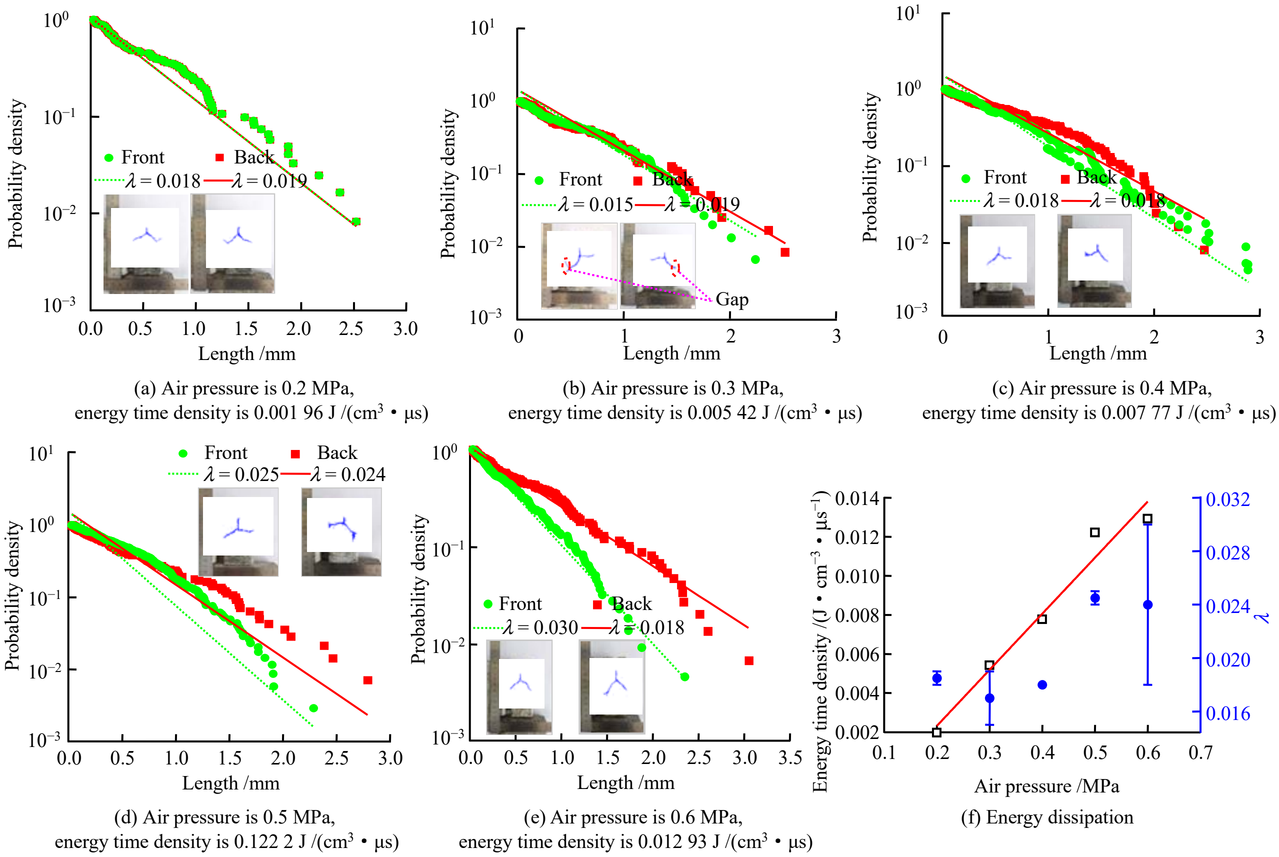


**Fig. 9 Quantitatively statistical results of cracks and energy dissipation**

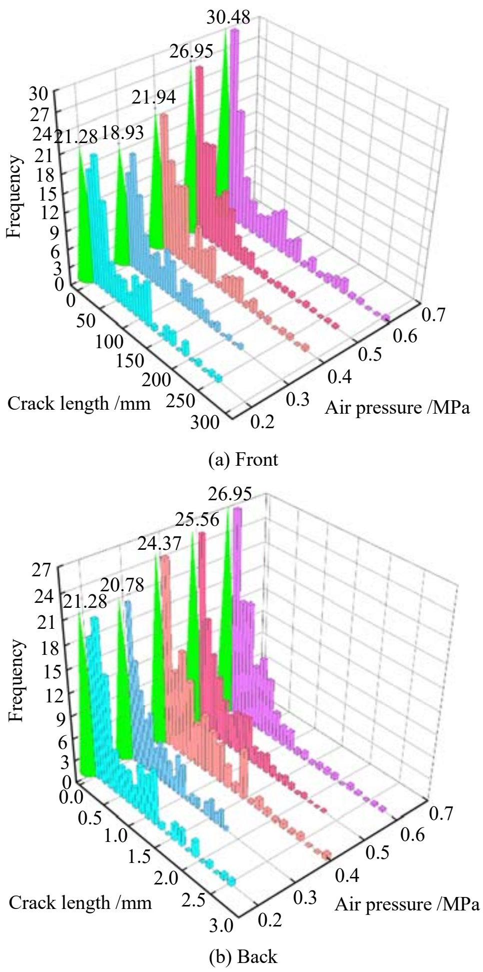


**Fig. 10 Statistics of crack length**

lengths in each group. In the overall trend, crack lengths ranging from 0 to 0.5 mm account for a large proportion, followed by cracks ranging from 0.5 mm to 1.0 mm, and the cracks larger than 1.5 mm share a small proportion. The results demonstrate a good crack connectivity. The crack width is narrow, and a few long straight lines can be combined to reconstruct a complete crack image. The high peak values of short cracks indicate the high degree of fracture of rock fracture surface. In addition, the peak frequency of the specimen on the back side appears in the range of 20.78–26.95 mm, close to the peak frequency appearing between 18.93–30.48 mm on the front side. The peak frequency is the lowest when the energy time density reaches 0.005 42 J /(cm$^3$ • μs) (air pressure of 0.3 MPa). The possible reason is that there is a notch at the edge of the specimen, and the crack extension is relatively long, while the fracture degree at the fracture surface is not high under low energy absorption, resulting in a minimum peak crack length after Hough transform. Another possible reason is that the impact pressure is low, so that the limited energy absorbed by the specimen leads to the generated fracture close to the prefabricated crack tip, giving rise to more short cracks under this pressure. Under other test conditions, the peak frequency is clustered at the crack length of 0.03 mm, while in the test with energy time density of 0.001 96 J /(cm$^3$ • μs) (air pressure of 0.2 MPa), the peak frequency is encountered

https://rocksoilmech.researchcommons.org/journal/vol44/iss7/1
DOI: 10.16285/j.rsm.2022.6209

at 0.15 mm. Under low pressure conditions, the cracks mainly consist of short and medium cracks. Generally, the peak frequency increases with the increase in air pressure. The peak crack lengths are 2.52, 2.25, 2.79, 2.73 and 3.05 mm on the front side, and 2.52, 1.79, 2.89, 2.29 and 2.73 mm on the back side. The reason for the large data discreteness is that the crack propagation direction of each group is different to some extent, and the peak crack length estimated by Hough transform is not the real crack length, which has little reference significance and results in data discreteness.

**4.2 Distribution of crack angles**

The rose diagrams in Fig. 11 show the distribution of crack angles. The true north direction N is defined as the specimen vertical direction, the corresponding angle is 90º, and the horizontal direction is defined as 0º. The distribution of crack angles presents a central symmetry. The peak frequencies in the front side group are 11.41, 8.53, 7.87, 10.54 and 7.72, respectively, while those in the back side group are 8.40, 11.79, 8.22, 8.64 and 8.02, respectively. The mean value is 10%. The distribution of crack angles is relatively concentrated, and the frequency of most angles is between 5% and 10%. In contrast, the proportion of crack angle in the horizontal direction is the least, which indicates that although the cracks coalesce at the left and right sides of the specimen, the horizontal cracks are scarce. In the test results of the front and back sides, the cracks at 90º (270º) only account for a small proportion, illustrating that the vertical crack development is insignificant. The cracks develop more obvious at the angles of 15º−60º and 105º−150º, proving that the crack direction deviates from the vertical direction of the specimen at a certain angle. In addition, when the energy time densities are 0.012 22 J /(cm$^3$ •μs) (air pressure of 0.5 MPa) and 0.012 93 J /(cm$^3$ • μs) (air pressure of 0.6 MPa), the angle distributions of the two groups of tests are relatively balanced, except for the vertical and horizontal directions. However, when the energy time densities are 0.001 96 J /(cm$^3$ • μs) (air pressure of 0.2 MPa), 0.005 42 J /(cm$^3$ • μs) (air pressure of 0.3 MPa) and 0.007 77 J /(cm$^3$ • μs) (air pressure of 0.4 MPa), the fluctuation of crack angles is more violent with some dominant directions appearing on the rose diagram of crack angle. It reveals that the directionality of cracks is less obvious and the bending degree of crack is larger in the case of high energy dissipation, whereas under low energy dissipation, the directional consistency of cracks is more prominent.

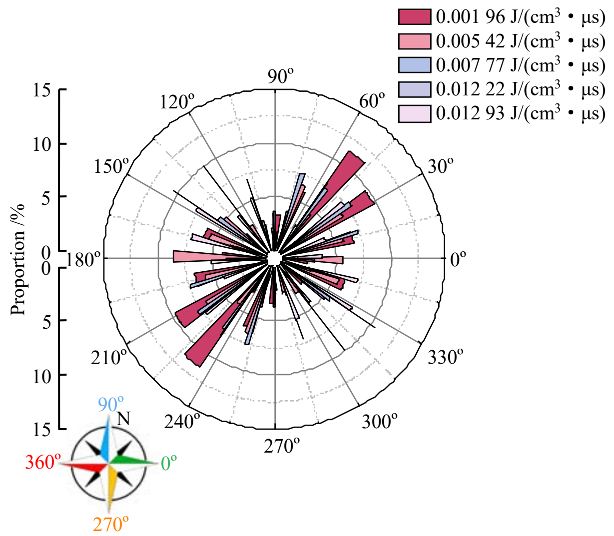


(a) Front

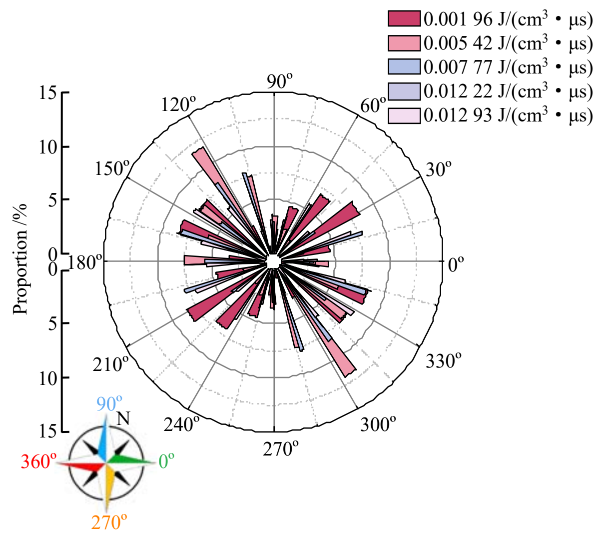


(b) Back

**Fig. 11 Statistics of crack angle**

Previous studies[10−12, 27] have shown that the growth process of prefabricated crack in the rock specimens under impact loading can be classified into three stages: cracks initiation, propagation and termination. In addition, the impact disturbance may lead to secondary initiation of cracks. In the results of five groups of tests, the direction of crack growth is significantly altered under the air pressure of 0.2−0.4 MPa, and the most obvious change occurs under the energy time density of 0.001 96 J /(cm$^3$ • μs) (air pressure of 0.2 MPa). As shown in Fig. 10(f), the absorbed energy increases linearly with the increase in air pressure. The energy absorbed by the SCT specimen is relatively small when the energy time density remains low. During the crack propagation, the phenomena of crack termination and secondary initiation occur, and the changing position is not far from the edge of the specimen. In addition, due to the heterogeneity of the granite in the preparation of the SCT specimen, the crack direction changes during secondary initiation of cracks, which is mainly caused by high energy dissipation. Therefore, in the test results of two groups of energy time densities of 0.007 77 J /(cm$^3$ • μs) (air pressure of 0.4 MPa) and 0.012 22 J /(cm$^3$ •μs)) (air pressure of 0.5 MPa), the crack termination and secondary initiation are rarely observed during the crack propagation along the main crack direction until coalescence.

In Figs. 8 and 11, although the cracks on the front and back sides of the specimen are symmetrical, the differences between the cracks on both sides are obvious, which are well demonstrated in the crack images and statistical results. In this regard, the absolute differences of crack length and angle are defined, representing the differences of crack length and angle between the front and back sides.

The absolute value of the crack length is calculated as

$$S_l = |L_{A1} - L_{A2}| + |L_{B1} - L_{B2}| \tag{9}$$

where $S_l$ is the sum of the absolute differences of crack length; $L$ is the crack length; and the subscripts A1, A2, B1 and B2 correspond to different crack numbers.

The absolute value of the crack angle can be obtained by

$$S_\theta = |\theta_{A1} - \theta_{A2}| + |\theta_{B1} - \theta_{B2}| \tag{10}$$

where $S_\theta$ is the sum of the absolute differences of the crack angle; and $\theta$ is the crack angle.

The statistics of crack length, crack angle and their absolute values are listed in Table 2, and the relationship between energy time density and absolute differences is plotted in Fig. 12.

**Table 2 Statistics of crack morphology**

| Air pressure /MPa | Energy time density /(J • cm$^{-3}$ • μs$^{-1}$) | Crack length at front side /mm | | Crack length at back side /mm | | Crack angle at front side /(°) | | Crack angle at back side /mm | | Absolute difference in length /mm | Absolute difference in angle /(°) |
|---|---|---|---|---|---|---|---|---|---|---|---|
| | | A1 | B1 | A2 | B2 | A1 | B1 | A2 | B2 | | |
| 0.2 | 0.001 96 | 23.1 | 26.2 | 24.1 | 24.8 | 60 | 45 | 75 | 50 | 2.4 | 20 |
| 0.3 | 0.005 42 | 41.9 | 26.5 | 37.4 | 21.0 | 50 | 90 | 45 | 75 | 10.0 | 20 |
| 0.4 | 0.007 77 | 34.1 | 25.2 | 36.5 | 20.2 | 55 | 55 | 45 | 60 | 7.4 | 15 |
| 0.5 | 0.012 22 | 29.4 | 28.0 | 31.5 | 21.0 | 55 | 75 | 45 | 75 | 9.1 | 10 |
| 0.6 | 0.012 93 | 25.8 | 28.2 | 33.0 | 31.0 | 55 | 45 | 55 | 40 | 10.0 | 5 |

As shown in Fig. 12, the absolute differences of crack length tend to increase with the increase in air pressure, but in the test with energy time density of 0.005 42 J /(cm$^3$ • μs) (air pressure of 0.3 MPa), the absolute differences are discrete, which may be caused by the notch on the front side of the specimen. It suggests that the more energy absorbed by the specimen, the more obvious the difference of cracks on both sides of the specimen. The absolute difference of crack angle of each group is close to each other, falling between 5º and 17º. In the test with energy time density of 0.012 93 J /(cm$^3$ • μs) (air pressure of 0.6 MPa), the absolute difference of crack angle is only 5º, indicating that the cracks on both sides of the specimen are closer to parallel under the test conditions. The results also confirm a low roughness of the fracture surface.

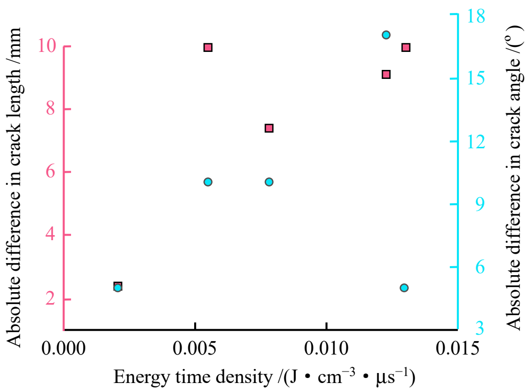


**Fig. 12 Relationship between energy time density and crack statistical results**

### 4.3 Statistical results

The statistical characteristics of a 3D fracture surface can be defined according to the indicators proposed by Belem et al.[25]:

$$Z_{2s} = \left\{ \frac{1}{L_x L_y} \int_0^{L_x} \int_0^{L_y} \left\{ \left[ \frac{\partial z(x,y)}{\partial x} \right]^2 + \left[ \frac{\partial z(x,y)}{\partial y} \right]^2 \right\} \mathrm{d}x\mathrm{d}y \right\}^{1/2} \tag{11}$$

Its approximation is expressed as

$$Z_{2s} = \left\{ \frac{1}{(N_x - 1)(N_y - 1)} \cdot \left[ \frac{1}{\Delta x^2} \sum_{i=1}^{N_x-1} \sum_{i=1}^{N_y-1} \frac{(z_{i+1,j+1} - z_{i,j+1})^2 + (z_{i+1,j} - z_{i,j})^2}{2} + \frac{1}{\Delta y^2} \sum_{i=1}^{N_y-1} \sum_{i=1}^{N_x-1} \frac{(z_{i+1,j+1} - z_{i+1,j})^2 + (z_{i,j+1} - z_{i,j})^2}{2} \right] \right\}^{\frac{1}{2}} \tag{12}$$

The 2D joint roughness coefficient (JRC) proposed by Barton et al.[32] is positively linear with the statistical function. However, the above studies all took the shear test as the research object, and the dimensions of the selected samples were 100 mm×100 mm×100 mm. In this study, the specimens are all in long strip shape with dimensions of 100 mm×50 mm×30 mm. The fracture surface size is set to 20 mm×30 mm, and the sampling interval of 1 mm seems to be too large, resulting in $Z_{2s}$ being too small. Figure 13 illustrates the variation of $Z_{2s}$ of fracture surface

A at different sampling intervals under energy time density of 0.001 96 J /(cm$^3$ • μs) (air pressure of 0.2 MPa).

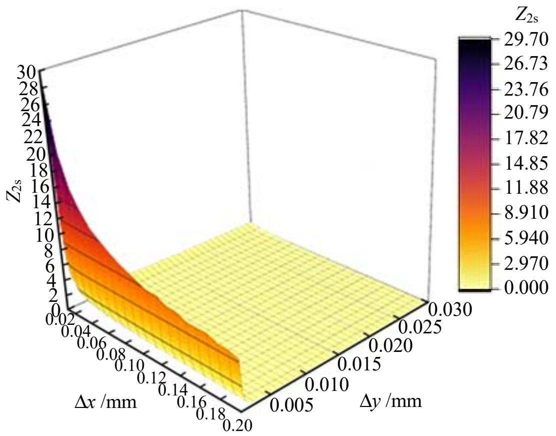


**Fig. 13 Relationship between sampling interval and $Z_{2s}$**

With the increase in sampling interval, $Z_{2s}$ decreases sharply until it approaches zero, showing an exponential decreasing trend. The peak $Z_{2s}$ is 29.66, corresponding to Δ*x* = 0.01 mm and Δ*y* = 0.1 mm, which is the minimum step size of the 3D topography detection device in the *x* and *y* directions. By summarizing the $Z_{2s}$ values of standard JRC curves in the literature, Yuan et al.[24] found that they were all between 0 and 1, and concluded that excessive sampling interval is obviously unreasonable. For the convenience of calculation, the sampling interval of Δ*x* = 0.1 mm and Δ*y* = 0.1 mm is assumed, and the obtained $Z_{2s}$ is 0.30. For the consistency of comparison, this sampling interval is also used in the calculation of other fracture surface statistical parameters.

The larger the value of $Z_{2s}$, the higher the roughness of rock fracture surface. As shown in Fig. 14, the correlation between the fracture surface roughness and air pressure is insignificant. However, the fracture surface roughness reaches the lowest under the air pressure of 0.6 MPa (energy time density of 0.012 93 J /(cm$^3$ • μs)), and the highest under the air pressure of 0.3 MPa (0.005 42 J /(cm$^3$ • μs)). The reason is that there is a noticeable notch on the left side of the specimen. The roughness parameter $Z_{2s}$ of

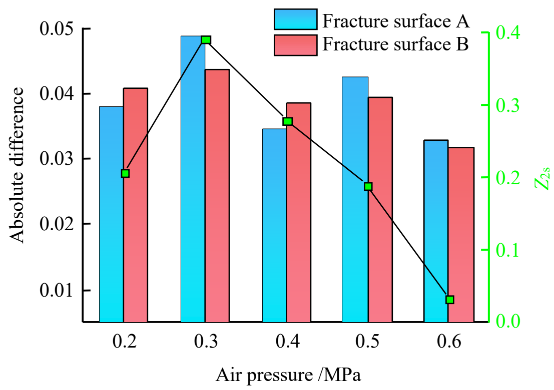


**Fig. 14 Relationship between air pressure and $Z_{2s}$**

fracture surface A is 0.40, while for other groups, $Z_{2s}$ values are similar. This is considered to be the outcome of crack termination and secondary initiation. In addition, the absolute differences of $Z_{2s}$ for fracture surfaces A and B were calculated, and the roughness difference of each group follows a decreasing trend except for the test under the air pressure of 0.2 MPa (0.001 96 J /(cm$^3$ • μs)). It shows that under high energy dissipation, the cracks in fracture surfaces A and B caused by impact loading coalesce well, the secondary initiation phenomenon is inconspicuous, and thus the difference in fracture surface roughness is negligible.

## 5 Conclusions

Based on the SHPB test system, this paper studied the dynamic fracture characteristics of SCT granite specimens, addressed the problem of removing error points in the 3D fracture surface point cloud data, and summarized the law of influence of impact load on the mode I crack morphology and fracture surface roughness. The main conclusions can be drawn as follow:

(1) The energy time density presents a positively linear relationship with the air pressure, and the functional relationship is $y$ = 0.028 73$x$−0.003 43 with $R^2$ = 0.97. With the increase in absorbed energy, the exponential distribution $\lambda$ of crack length increases. Overall, the cracks with the length of 0−0.5 mm are the most, followed by the cracks with the length of 0.5−1.0 mm, and the proportion of cracks greater than 1.5 mm is the least.

(2) Morphologically, the cracks coalesce on the left and right sides of the specimen, and the horizontal cracks are less developed. The distribution of crack angles has no prominent direction, except at low energy time density, at which crack termination and secondary initiation would occur. At high energy time density, the cracks have the characteristics of higher bending degree, less obvious directionality, and good connectivity.

(3) The fitting surface threshold detection method is used to remove the error points and reconstruct the fracture surface data. It is found that the reasonable value of the fitting surface in the *x* and *y* directions is between 0.03 and 0.08, and the threshold is 0.25. The difference in roughness parameter of each group experiences a decreasing trend with the increase in energy time density, and the cracks of fracture surfaces A and B coalesce well at high energy time density.

### References

[1] FAN Jie, ZHU Xing, HU Ju-wei, et al. Experimental study on crack propagation and damage monitoring of sandstone using three-dimensional digital image correlation technology[J]. Rock and Soil Mechanics, 2022, 43(4): 1009−1019.

[2] YANG En-guang, YANG Li-yun, HU Huan-ning, et al. Experimental and numerical research on propagation of closed cracks under uniaxial compression[J]. Rock Mechanics and Rock Engineering, 2022: 1−11.

[3] HE M, ZHANG Z, ZHENG J, et al. A new perspective on the constant $m_i$ of the Hoek–Brown failure criterion and a new model for determining the residual strength of rock[J]. Rock Mechanics and Rock Engineering, 2020, 53(9): 3953−3967.

[4] LÜ N, WANG H, RONG K, et al. The numerical simulation of large diameter split Hopkinson pressure bar and Hopkinson bundle bar of concrete based on mesoscopic model[J]. Construction and Building Materials, 2022, 315: 125728.

[5] YAN Z, DAI F, LIU Y, et al. Dynamic strength and cracking behaviors of single-flawed rock subjected to coupled static–dynamic compression[J]. Rock Mechanics and Rock Engineering, 2020, 53(9): 4289−4298.

[6] GONG F, SI X, LI X, et al. Dynamic triaxial compression tests on sandstone at high strain rates and low confining pressures with split Hopkinson pressure bar[J]. International Journal of Rock Mechanics and Mining Sciences, 2019, 113: 211−219.

[7] LI X F, LI X, LI H B, et al. Dynamic tensile behaviours of heterogeneous rocks: the grain scale fracturing characteristics on strength and fragmentation[J]. International Journal of Impact Engineering, 2018, 118: 98−118.

[8] WANG Fei, WANG Meng, ZHU Zhe-ming, et al. Study on evolution law of rock crack dynamic propagation in complete process under impact loading[J]. Chinese Journal of Rock Mechanics and Engineering, 2019, 38(6): 1139−1148.

[9] CAO Fu, YANG Li-ping P, LI Lian, et al. Research on whole dynamical fracture process of rock using single cleavage drilled compression (SCDC) specimen[J]. Rock and Soil Mechanics, 2017, 38(6): 1573−1582.

[10] NI Min, GOU Xiao-ping, WANG Qi-zhi. Stress intensity factor formulas for DCDC and SCDC specimens[J]. Chinese Journal of Theoretical and Applied Mechanics, 2013, 45(1): 9.

[11] NI Min, GOU Xiao-ping, WANG Qi-zhi. Test method for rock dynamic fracture toughness using single cleavage drilled compression specimen impacted[J]. Engineering Mechanics, 2013, 30(1): 365−372.

[12] DONG Yu-qing, ZHU Zhe-ming, WANG Meng, et al. Mode I crack dynamic propagation behavior of SCT specimens under medium-low speed impact load[J]. Journal of Central South University (Science and Technology), 2018, 49(11): 2821−2830.

[13] DONG Y Q, ZHU Z M, ZHOU L, et al. Study of mode I crack dynamic propagation behaviour and rock dynamic fracture toughness by using SCT specimens[J]. Fatigue & Fracture of Engineering Materials & Structures, 2018, 41(8): 1810−1822.

[14] WANG Xing-yu, ZHU Zhe-ming, QIU Hao, et al. Study of the effect of stratifications on crack propagation behaviors in shale under impacting loads[J]. Chinese Journal of Rock Mechanics and Engineering, 2019, 38(8): 1542−1556.

[15] WANG X Y, ZHU Z M, ZHOU L, et al. Study on the effects of joints orientation and strength on failure behavior in shale specimen under impact loads[J]. International Journal of Impact Engineering, 2022, 163: 104162.

[16] HOUGH P V. Method and means for recognizing complex patterns[J]. US Patent, 1962, 3(6): 1−10.

[17] CUI Yan, ZHOU Xin-chang, LIU Ya-fei, et al. Solar meridian extraction method based on hough transformation[J]. Acta Optica Sinica, 2020, 40(17): 14−20.

[18] QIN Ruo-lin, JIANG Xiao-gang, JIN Liang-an, et al. Study of characteristics extraction of underwater bubbles group based on Hough transform[J]. Acta Armamentarii, 2019, 40(12): 2504−2512.

[19] SHI Feng-yuan, ZHENG Xun-jiang, JIANG Li-hui, et al. Point cloud registration algorithm for non-cooperative targets based on Hough transform[J]. Journal of Beijing University of Aeronautics and Astronautics, 2022, doi: 10.13700/j.bh.1001-5965.2021.0575.

[20] DAVID H, RIZZO R E, CORNWELL D G, et al. FracPaQ: A MATLAB™ toolbox for the quantification of fracture patterns[J]. Journal of Structural Geology, 2017, 95: 1−16.

[21] RIZZO R E, HEALY D, HEAP M J, et al. Detecting the onset of strain localization using two-dimensional wavelet analysis on sandstone deformed at different effective pressures[J]. Journal of Geophysical Research: Solid Earth, 2018, 123(12): 410−460, 478.

[22] RIZZO R E, HEALY D, FARRELL N J, et al. Riding the right wavelet: quantifying scale transitions in fractured rocks[J]. Geophysical Research Letters, 2017, 44(23): 808−811, 815.

[23] CHEN Shi-jiang, ZHU Wan-cheng, WANG Chuang-ye, et al. Review of research progresses of the quantifying joint roughness coefficient[J]. Chinese Journal of Theoretical and Applied Mechanics, 2017, 49(2): 239−256.

[24] YUAN Zhou-hao, YE Yi-cheng, LUO Bin-yu, et al. Hierarchical characterization joint surface roughness coefficient of rock joint based on wavelet transform[J]. Journal of China Coal Society, 2021: 1−19.

[25] BELEM T, HOMAND-ETIENNE F, SOULEY M. Quantitative parameters for rock joint surface roughness[J]. Rock Mechanics and Rock Engineering, 2000, 33(4): 217−242.

[26] LIU X G, ZHU W C, YU Q L, et al. Estimation of the joint roughness coefficient of rock joints by consideration of two-order asperity and its application in double-joint shear tests[J]. Engineering Geology, 2017, 220: 243−255.

[27] XIA Cai-chu, WANG Wei, DING Zeng-zhi. Development of three-dimensional TJXW–3D-typed portable rock surface topography[J]. Chinese Journal of Rock Mechanics and Engineering, 2008, 27(7): 1505−1512.

[28] CHEN Xi, ZENG Ya-wu. A new three-dimensional roughness metric based on Grasselli's model[J]. Rock and Soil Mechanics, 2021, 42(3): 700−712.

[29] WANG X, GUO L, XU Z, et al. A new index of energy dissipation considering time factor under the impact loads[J]. Materials, 2022, 15(4): 1443.

[30] TATONE B S. Quantitative characterization of natural rock discontinuity roughness in-situ and in the laboratory[M]. Toronto: [s. n.], 2009.

[31] GRASSELLI G, EGGER P. Constitutive law for the shear strength of rock joints based on three-dimensional surface parameters[J]. International Journal of Rock Mechanics and Mining Sciences, 2003, 40(1): 25−40.

[32] BARTON N, CHOUBEY V. The shear strength of rock joints and practice[J]. Rock Mechanics, 1977, 10(1−2): 1−54.